Topological magnon polarons in honeycomb antiferromagnets with spin-flop transition

Gyungchoon Go,[1] Heejun Yang,[2] Je-Geun Park,[2] and Se Kwon Kim[1]
[1]*Department of Physics, Korea Advanced Institute of Science and Technology, Daejeon 34141, South Korea*
[2]*Department of Physics and Astronomy, Seoul National University, Seoul 08826, South Korea*

(Received 29 January 2024; revised 17 April 2024; accepted 6 May 2024; published 21 May 2024)

We theoretically investigate the thermal Hall transport of magnon-polarons in a two-dimensional honeycomb antiferromagnetic insulator under the influence of a perpendicular magnetic field, varying in strength. The application of a perpendicular magnetic field induces a magnetic phase transition from the collinear antiferromagnetic phase to the spin-flop phase, leading to a significant alteration in Hall transport across the transition point. In this paper, our focus is on the intrinsic contribution to thermal Hall transport arising from the magnetoelastic interaction. To facilitate experimental verification of our theoretical results, we present the dependence of thermal Hall conductivity on magnetic field strength and temperature.

DOI: 10.1103/PhysRevB.109.184435

I. INTRODUCTION

In recent years, intrinsic magnetism in two-dimensional (2D) insulators has been discovered, attracting growing attention, driven by its fundamental interest and technological applications in reduced dimensions [1–12]. Within magnetic insulators, magnetic excitations (magnons) and lattice vibrations (phonons) serve as carriers of energy and information. The exploration of these collective, charge-neutral, low-energy excitations has attracted considerable interest due to their potential for innovative approaches to manipulate and control thermal energy and information [13,14]. A particular focus lies on the topological Hall transport of collective excitations resulting from Berry curvature. Previous research has demonstrated the magnon Hall effect in chiral magnetic systems with chiral spin texture [15–19], or Dzyaloshinskii-Moriya interaction [20–28]. Additionally, studies have explored the phonon Hall effect arising from the interaction between phonons and static magnetization [29–31], or scattering from the impurities [32–34]. Beyond individual magnons and phonons, their hybrid excitations known as magnon-polarons potentially exhibit topological properties through the long-range dipolar interaction [35], the Dzyaloshinskii-Moriya interaction [36–39], and strain-dependent magnetic anisotropy [40–45].

The strain-dependent magnetic anisotropy is a well-known mechanism of magnetoelastic interaction and magnetostriction [46–48], ubiquitous in magnetic materials. Recent experiments have revealed its role in opening band gaps between magnon and phonon modes [49,50] and inducing the topological transport of the quasiparticles [38,51,52]. Most theoretical investigations into the magnetoelastic interaction-induced topological magnon-polaron have focused on collinear magnetic systems, where the magnetic order aligns in the uniform direction. Consequently, they are not directly applicable to certain antiferromagnetic (AFM) systems, including the spin-flop ground state. In the spin-flop phase of bipartite antiferromagnets, two spins on the two sublattices tilt at an angle $\theta_A = \theta_B$ (Fig. 1). In the tilted ground state, magnons couple not only with out-of-plane phonons but also with in-plane phonons [42]. However, a theoretical investigation of topological magnon-polaron bands, including both in-plane and out-of-plane phonon modes in the AFM spin-flop state, is currently lacking.

In this paper, we investigate the topological properties of the magnon-polarons in a two-dimensional honeycomb antiferromagnet subjected to a variable magnetic field induced by the magnetoelastic interaction. More specifically, we compute the band structures and topological properties of the magnon-polarons in both collinear AFM and spin-flop states. To facilitate further comparison with experimental studies, we calculate the magnetic field dependence of the thermal Hall conductivity at different temperatures.

The remaining sections of this paper are organized as follows. In Sec. II, we present model Hamiltonians for magnons, phonons, and magnetoelastic interaction in both collinear AFM and spin-flop states. In Sec. III, we calculate the band structures and Berry curvatures of the magnon-polaron bands. In Sec. IV, we compute the the thermal Hall conductivity of the magnon-polarons. In Sec. V, we conclude by providing a brief summary and discussion.

II. MODEL HAMILTONIAN

A. Magnon part

Here, we consider the spin Hamiltonian for a 2D honeycomb AFM system, given by

$$H_m = J\sum_{\langle i,j\rangle}\mathbf{S}_i\cdot\mathbf{S}_j - K\sum_i (S_{i,z})^2 - b\sum_i S_{i,z}, \qquad (1)$$

where the first and second term are the antiferromagnetic exchange interaction ($J > 0$) and the easy-axis anisotropy ($K > 0$), respectively. For simplicity, in the analytic calculation within this section, we exclusively focus on nearest-neighbor exchange. In the numerical analysis (Secs. III and IV), we integrate the second- and third-nearest-neighbor exchanges (J_2 and J_3) to properly capture the magnon dynamics [25,53,54].

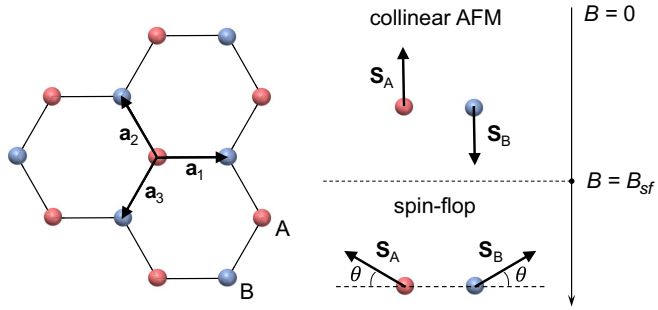

FIG. 1. Schematic illustration of the honeycomb lattice (left). Equilibrium spin configurations depending on external magnetic field (right).

The parameter $b(= g\mu_B B)$ in the last term represents the external magnetic field along z direction, where g is the the g factor, and μ_B is the Bohr magneton. The nearest-neighbor vectors are $\mathbf{a}_1 = a(1, 0)$, $\mathbf{a}_2 = \frac{a}{2}(-1, \sqrt{3})$, and $\mathbf{a}_3 = -\frac{a}{2}(1, \sqrt{3})$. The next-nearest-neighbor vector are defined as $\mathbf{b}_1 = \mathbf{a}_1 - \mathbf{a}_3$, $\mathbf{b}_2 = \mathbf{a}_2 - \mathbf{a}_1$, and $\mathbf{b}_3 = \mathbf{a}_3 - \mathbf{a}_1$ (see Fig. 1).

A sufficiently strong magnetic field B destabilizes the collinear AFM order, leading to a spin-flop phase transition, which is a first-order reorientation transition [55]. For $B < B_{\rm sf}$, where

$$B_{\rm sf} = \frac{2S\sqrt{(3J - K)K}}{g\mu_B}, \tag{2}$$

the equilibrium spin configuration forms a collinear AFM state along the z axis. In the spin-flop phase ($B > B_{\rm sf}$), the spin directions of the two sublattices are canted along the field direction (see Fig. 1). Below, we compute the magnon spectra for these two distinct equilibrium spin configurations.

1. Magnon Hamiltonian in a collinear AFM state

In the collinear AFM state with the spin configuration $\mathbf{S}_{i\in A} = S\hat{\mathbf{z}}$ and $\mathbf{S}_{i\in B} = -S\hat{\mathbf{z}}$, we perform the Holstein-Primakoff transformation and take the Fourier transformation, leading to the magnon Hamiltonian,

$$H_m = \frac{1}{2}\sum_{\mathbf{k}} \psi^\dagger_{m,\mathbf{k}} \mathcal{H}_m(\mathbf{k}) \psi_{m,\mathbf{k}}, \tag{3}$$

where $\psi_{m,\mathbf{k}} = (a_{\mathbf{k}}, b_{\mathbf{k}}, a^\dagger_{-\mathbf{k}}, b^\dagger_{-\mathbf{k}})^T$ is the basis function and the momentum space Hamiltonian is given by

$$\mathcal{H}^m_{\mathbf{k}} = JS \begin{pmatrix} 3+\kappa_+ & 0 & 0 & f_{\mathbf{k}} \\ 0 & 3+\kappa_- & f^*_{\mathbf{k}} & 0 \\ 0 & f_{\mathbf{k}} & 3+\kappa_+ & 0 \\ f^*_{\mathbf{k}} & 0 & 0 & 3+\kappa_- \end{pmatrix}, \tag{4}$$

where $\kappa_\pm = (2K \pm b/S)/J$ and $f_{\mathbf{k}} = \sum_j e^{i\mathbf{k}\cdot\mathbf{a}_j}$. To diagonalize the Bogoliubov Hamiltonian, we find the paraunitary matrix $U_{\mathbf{k}}$ satisfying $E_{\mathbf{k}} = U^\dagger_{\mathbf{k}} \mathcal{H}_{\mathbf{k}} U_{\mathbf{k}} = \mathrm{diag}(\epsilon_{\mathbf{k}}, \epsilon_{-\mathbf{k}})$. Following the notation used in Ref. [28], we write the eigenvalue equations

$$\begin{aligned} \sigma_3 \mathcal{H}_{\mathbf{k}} |u^R_{n,\mathbf{k}}\rangle &= \bar{\epsilon}_{n,\mathbf{k}} |u^R_{n,\mathbf{k}}\rangle, \\ \langle u^L_{n,\mathbf{k}}| \sigma_3 \mathcal{H}_{\mathbf{k}} &= \bar{\epsilon}_{n,\mathbf{k}} \langle u^L_{n,\mathbf{k}}|, \end{aligned} \tag{5}$$

where $\sigma_3 = \mathrm{diag}(1, 1, -1, -1)$ is the Pauli matrix acting on the particle-hole space. Here $\langle u^L_{n,\mathbf{k}}| = \langle u^R_{n,\mathbf{k}}|\sigma_3$ and $|u^R_{n,\mathbf{k}}\rangle = U_{n,\mathbf{k}}$ are the left and right eigenvectors of the pseudo-Hermitian Hamiltonian $\sigma_3\mathcal{H}_{\mathbf{k}}$, respectively. The orthonormal relation of the eigenvectors reads $\langle u^L_{n,\mathbf{k}}|u^R_{m,\mathbf{k}}\rangle = \langle u^R_{n,\mathbf{k}}|\sigma_3|u^R_{m,\mathbf{k}}\rangle = (\sigma_3)_{nm}$ and the pseudo-eigenvalue satisfies $\bar{\epsilon}_{n,\mathbf{k}} = (\sigma_3\epsilon_{\mathbf{k}})_{nn}$. By solving Eq. (5), we determine the energy eigenvalues of the magnon bands,

$$\epsilon^{\rm AFM,\pm}_{m,\mathbf{k}} = JS\sqrt{(3+\kappa)^2 - |f_{\mathbf{k}}|^2} \pm b, \tag{6}$$

where $\kappa = 2K/J$. The two magnonic states, denoted as–and +, carry opposite spin angular momenta, with $S_z = -1$ and $S_z = +1$, respectively.

2. Magnon Hamiltonian in a spin-flop state

In the spin-flop phase, the equilibrium spin configuration is

$$\begin{aligned} \mathbf{S}_A &= S(-\cos\theta, 0, \sin\theta), \\ \mathbf{S}_B &= S(\cos\theta, 0, \sin\theta), \end{aligned} \tag{7}$$

where $\theta = \sin^{-1}(\frac{b}{2(3J-K)S})$ is the canted angle. Here we assume the equilibrium spin profile lies in the xz plane, for simplicity. To investigate the spin-wave dynamics in the canted AFM phase, we introduce the sublattice dependent coordinate system ($\mathbf{S}'_\alpha$) where the equilibrium spin direction is along the z axis [56]

$$\mathbf{S}_\alpha = \begin{pmatrix} \sin\theta & 0 & (-1)^{\nu+1}\cos\theta \\ 0 & 1 & 0 \\ (-1)^\nu \cos\theta & 0 & \sin\theta \end{pmatrix} \mathbf{S}'_\alpha, \tag{8}$$

where $\nu = 1, 2$ is the sublattice index ($A = 1, B = 2$). By substituting the new spin variables into Eq. (1), and neglecting the magnon-magnon interaction terms, we obtain the low-energy Hamiltonian describing linear spin waves [26]

$$\begin{aligned} H = &-J\sum_{\langle i,j\rangle} \left[\cos 2\theta \left(S'^x_i S'^x_j + S'^z_i S'^z_j\right) - S'^y_i S'^y_j\right] \\ &- K\sum_i \left[\left(S'^z_i\right)^2 \sin^2\theta + \left(S'^x_i\right)^2 \cos^2\theta\right] - b\sum_i S'^z_i. \end{aligned} \tag{9}$$

The Holstein-Primakoff approach yields the Bogoliubov Hamiltonian

$$\mathcal{H}^m_{\mathbf{k}} = \begin{pmatrix} I_K & F_{1,\mathbf{k}} & K_0 & F_{2,\mathbf{k}} \\ F^*_{1,\mathbf{k}} & I_K & F^*_{2,\mathbf{k}} & K_0 \\ K_0 & F_{2,\mathbf{k}} & I_K & F_{1,\mathbf{k}} \\ F^*_{2,\mathbf{k}} & K_0 & F^*_{1,\mathbf{k}} & I_K \end{pmatrix}, \tag{10}$$

where

$$\begin{aligned} I_K &= 3JS\cos 2\theta + KS(2\sin^2\theta - \cos^2\theta) + b\sin\theta, \\ F_{1,\mathbf{k}} &= JSf_{\mathbf{k}}\sin^2\theta, \quad F_{2,\mathbf{k}} = -JSf_{\mathbf{k}}\cos^2\theta, \\ K_0 &= -KS\cos^2\theta. \end{aligned} \tag{11}$$

By solving the eigenvalue equation in the particle-hole space, we obtain the magnon band dispersion

$$\epsilon^{\rm SF,\pm}_{m,\mathbf{k}} = \sqrt{(I^-_K \pm JS|f_{\mathbf{k}}|)(I^+_K \mp JS|f_{\mathbf{k}}|\cos 2\theta)}, \tag{12}$$

where $I_K^{\pm} = I_K \pm K_0$. It is noteworthy that the azimuthal angle of the equilibrium state is arbitrarily chosen in the spin-flop phase, leading to the breaking of U(1) spin-rotational symmetry. For $\mathbf{k} = 0$, the low-energy magnonic mode $\epsilon^{\mathrm{SF},-}_{m,\mathbf{k}=0} = 0$ is the gapless mode associated with spontaneous breaking of the U(1) symmetry, while the high-energy mode $\epsilon^{\mathrm{SF},+}_{m,\mathbf{k}=0} \approx \sqrt{b^2 - 12JKS^2}$ corresponds to the quasi-ferromagnetic resonance mode [57,58].

B. Phonon part

The elastic Hamiltonian describing the lattice dynamics can be written as

$$H_p = \sum_i \frac{\mathbf{p}_i^2}{2M} + \frac{1}{2}\sum_{i,j,\alpha,\beta} u_i^{\alpha}\Phi_{i,j}^{\alpha,\beta}u_j^{\beta}, \tag{13}$$

where $\mathbf{u}_i$ is the displacement vector of the ith ion from its equilibrium position, $\mathbf{p}_i$ is the conjugate momentum vector, M is ion mass, and $\Phi_{i,j}^{\alpha,\beta}$ is a force constant matrix. By using the Fourier transformation, we obtain the momentum space Hamiltonian

$$H_p = \sum_{\mathbf{k}}\left[\frac{p_{-\mathbf{k}}^{\alpha}p_{\mathbf{k}}^{\alpha}}{2M} + \frac{1}{2}u_{-\mathbf{k}}^{\alpha}\Phi(\mathbf{k})^{\alpha\beta}u_{\mathbf{k}}^{\beta}\right]. \tag{14}$$

By introducing the dimensionless variables $\bar{u}_{\mathbf{k}}^{\alpha} = \sqrt{\frac{M\omega_0}{\hbar}}u_{\mathbf{k}}^{\alpha}$ and $\bar{p}_{\mathbf{k}}^{\alpha} = \frac{1}{\sqrt{M\hbar\omega_0}}p_{\mathbf{k}}^{\alpha}$, we rewrite the Hamiltonian (14) as

$$H_p = \frac{1}{2}\sum_{\mathbf{k}}\psi_{p,\mathbf{k}}^{\dagger}\mathcal{H}_{\mathbf{k}}^{p}\psi_{p,\mathbf{k}}, \tag{15}$$

where the momentum space Hamiltonian is

$$\mathcal{H}_{\mathbf{k}}^{p} = \begin{pmatrix} \frac{\hbar}{M\omega_0}\Phi(\mathbf{k}) & 0 \\ 0 & \hbar\omega_0 I_{6\times 6}\end{pmatrix}. \tag{16}$$

and the basis function is

$$\begin{aligned}\psi_{p,\mathbf{k}} &= \big(\bar{u}_{x,\mathbf{k}}^{A}, \bar{u}_{y,\mathbf{k}}^{A}, \bar{u}_{z,\mathbf{k}}^{A}, \bar{u}_{x,\mathbf{k}}^{B}, \bar{u}_{y,\mathbf{k}}^{B}, \\ &\quad\times \bar{u}_{z,\mathbf{k}}^{B}, \bar{p}_{x,\mathbf{k}}^{A}, \bar{p}_{y,\mathbf{k}}^{A}, \bar{p}_{z,\mathbf{k}}^{A}, \bar{p}_{x,\mathbf{k}}^{B}, \bar{p}_{y,\mathbf{k}}^{B}, \bar{p}_{z,\mathbf{k}}^{B}\big)^{T},\ \psi_{p,\mathbf{k}}^{\dagger} \\ &= \psi_{p,-\mathbf{k}}.\end{aligned} \tag{17}$$

The momentum space representation of the force constant matrix is expressed as

$$\Phi(\mathbf{k}) = \begin{pmatrix}\Phi^{AA}(\mathbf{k}) & \Phi^{AB}(\mathbf{k}) \\ \Phi^{BA}(\mathbf{k}) & \Phi^{BB}(\mathbf{k})\end{pmatrix}, \tag{18}$$

where $\Phi^{AB}(\mathbf{k}) = \Phi^{BA}(-\mathbf{k})$ represents the elastic interaction between different sublattices from the nearest-neighbor couplings. In the first- and second-neighbor approximation of the 2D honeycomb lattice, the in-plane and out-of-plane phonon modes do not couple [59], and the momentum space force constant matrix between the nearest-neighbors is given by

$$\begin{aligned}\Phi_{ij}^{AB}(\mathbf{k}) &= \Phi_{ij}^{AB}(\mathbf{a}_1)e^{ik_x a} + \Phi_{ij}^{AB}(\mathbf{a}_2)e^{i(-\frac{k_x a}{2} + \frac{\sqrt{3}k_y a}{2})} \\ &\quad + \Phi_{ij}^{AB}(\mathbf{a}_3)e^{i(-\frac{k_x a}{2} - \frac{\sqrt{3}k_y a}{2})},\end{aligned} \tag{19}$$

where i and j represent phonon modes in cartesian coordinates, i.e., $\{i, j\} \in (x, y, z)$. The first component of the force constant matrix in Eq. (19) is given by

$$\Phi_{ij}^{AB}(\mathbf{a}_1) = \begin{pmatrix} K_L & 0 & 0 \\ 0 & K_T & 0 \\ 0 & 0 & K_Z\end{pmatrix}. \tag{20}$$

The other components are obtained by the C_3 rotation around z axis [59]

$$\Phi_{ij}^{AB}(\mathbf{a}_m) = U_m^{-1}\Phi_{ij}^{AB}(\mathbf{a}_1)U_m, \qquad (m = 2, 3) \tag{21}$$

where

$$U_m = \begin{pmatrix} \cos\theta_m & \sin\theta_m & 0 \\ -\sin\theta_m & \cos\theta_m & 0 \\ 0 & 0 & 1\end{pmatrix}, \tag{22}$$

with $\theta_2 = \frac{2\pi}{3}$ and $\theta_3 = -\frac{2\pi}{3}$. Therefore, we have

$$\Phi^{AB}(\mathbf{k}) = \begin{pmatrix}\Phi_{xx}^{AB}(\mathbf{k}) & \Phi_{xy}^{AB}(\mathbf{k}) & 0 \\ \Phi_{yx}^{AB}(\mathbf{k}) & \Phi_{yy}^{AB}(\mathbf{k}) & 0 \\ 0 & 0 & \Phi_{zz}^{AB}(\mathbf{k})\end{pmatrix}, \tag{23}$$

where

$$\begin{aligned}\Phi_{xx}^{AB}(\mathbf{k}) &= K_L e^{ik_x} + \frac{1}{2}(K_L + 3K_T)e^{-\frac{ik_x}{2}}\cos\left(\frac{\sqrt{3}}{2}k_y\right), \\ \Phi_{xy}^{AB}(\mathbf{k}) &= \Phi_{yx}^{AB}(\mathbf{k}) = i\frac{\sqrt{3}}{2}(K_T - K_L)e^{-\frac{ik_x}{2}}\sin\left(\frac{\sqrt{3}}{2}k_y\right), \\ \Phi_{yy}^{AB}(\mathbf{k}) &= K_T e^{ik_x} + \frac{1}{2}(3K_L + K_T)e^{-\frac{ik_x}{2}}\cos\left(\frac{\sqrt{3}}{2}k_y\right), \\ \Phi_{zz}^{AB}(\mathbf{k}) &= K_Z f_{\mathbf{k}}.\end{aligned} \tag{24}$$

The diagonal elements of the force constant matrices are

$$\Phi^{AA}(\mathbf{k}) = \Phi^{BB}(\mathbf{k}) = 3\begin{pmatrix}\frac{K_L+K_T}{2} & 0 & 0 \\ 0 & \frac{K_L+K_T}{2} & 0 \\ 0 & 0 & K_Z\end{pmatrix}, \tag{25}$$

which ensures that the lowest energy of the acoustic phonon modes remains zero.

C. Magnon-phonon interaction Hamiltonian

The general expression of the magnetoelastic interaction is given by [46,47]

$$H_{mp} = -\sum_i \mathbf{S}_i^T E_i \mathbf{S}_i = -\sum_{\nu}\sum_{i\in\nu}\mathbf{S}_{\nu,i}^T E_i^{\nu}\mathbf{S}_{\nu,i}, \tag{26}$$

where $\nu = 1, 2$ is the sublattice index ($A = 1, B = 2$). The coupling matrix is written in terms of the cartesian strain tensor,

$$\epsilon_{\alpha\beta}^{i} = \frac{1}{2}\left(\frac{\partial u_i^{\beta}}{\partial r_{\alpha}} + \frac{\partial u_i^{\alpha}}{\partial r_{\beta}}\right). \tag{27}$$

In the hexagonal systems, the magnetoelastic Hamiltonian in Ref. [48] leads to

$$E_i^{\nu} = \frac{1}{2}\begin{pmatrix} B^{\gamma}\epsilon_1^{\gamma} & B^{\gamma}\epsilon_2^{\gamma} & B^{\epsilon}\epsilon_2^{\epsilon} \\ B^{\gamma}\epsilon_2^{\gamma} & -B^{\gamma}\epsilon_1^{\gamma} & B^{\epsilon}\epsilon_1^{\epsilon} \\ B^{\epsilon}\epsilon_2^{\epsilon} & B^{\epsilon}\epsilon_1^{\epsilon} & \sqrt{3}\big(B_{12}^{\alpha}\epsilon_1^{\alpha} + B_{22}^{\alpha}\epsilon_2^{\alpha}\big)\end{pmatrix}, \tag{28}$$

where $\epsilon_1^\alpha = \epsilon_{xx} + \epsilon_{yy} + \epsilon_{zz}$, $\epsilon_2^\alpha = \frac{\sqrt{3}}{2}(\epsilon_{zz} - \frac{1}{3}\epsilon_1^\alpha)$, $\epsilon_1^\gamma = \frac{1}{2}(\epsilon_{xx} - \epsilon_{yy})$, $\epsilon_2^\gamma = \epsilon_{xy}$, $\epsilon_1^\epsilon = \epsilon_{yz}$, and $\epsilon_2^\epsilon = \epsilon_{xz}$ are the symmetrized strains in the hexagonal point group. In a discrete system, the local strains can be written as [44,60]

$$\epsilon_{\alpha\beta}^i \to \bar{\epsilon}_{\alpha\beta}^{i,\nu} = \frac{1}{n}\sum_{m=1}^{3} \bar{\epsilon}_{\alpha\beta}^{i,i+\mathbf{a}_m^D}, \tag{29}$$

where $\mathbf{a}_m^\nu$ is the nearest-neighbor vector ($\mathbf{a}_m^A = -\mathbf{a}_m^B$), and the components of the strain tensor are

$$\bar{\epsilon}_{\alpha\beta}^{i,i+\mathbf{a}_m^\nu} = \tfrac{1}{2}\left[a_m^{\nu,\alpha}\left(u_i^\beta - u_{i+\mathbf{a}_m^\nu}^\beta\right) + a_m^{\nu,\beta}\left(u_i^\alpha - u_{i+\mathbf{a}_m^\nu}^\alpha\right)\right], \tag{30}$$

where n is a normalization constant that ensures $\bar{\epsilon}_{\alpha\beta}^{i,\nu}$ reduced to $\epsilon_{\alpha\beta}^i$ in the long-wavelength limit (in honeycomb lattice $n = -3a^2/2$). The explicit expression for the local strain components is given by

$$\begin{aligned}
\bar{\epsilon}_{xx}^{i,A} &= -\frac{1}{3a}\left(-2u_{B,i+\mathbf{a}_1}^x + u_{B,i+\mathbf{a}_2}^x + u_{B,i+\mathbf{a}_3}^x\right),\\
\bar{\epsilon}_{yy}^{i,A} &= -\frac{1}{\sqrt{3}a}\left(-u_{B,i+\mathbf{a}_2}^y + u_{B,i+\mathbf{a}_3}^y\right),\\
\bar{\epsilon}_{xy}^{i,A} &= -\frac{1}{6a}\Big(-2u_{B,i+\mathbf{a}_1}^y + u_{B,i+\mathbf{a}_2}^y + u_{B,i+\mathbf{a}_3}^y\\
&\quad - \sqrt{3}u_{B,i+\mathbf{a}_2}^x + \sqrt{3}u_{B,i+\mathbf{a}_3}^x\Big),\\
\bar{\epsilon}_{xz}^{i,A} &= -\frac{1}{6a}\left(-2u_{B,i+\mathbf{a}_1}^z + u_{B,i+\mathbf{a}_2}^z + u_{B,i+\mathbf{a}_3}^z\right),\\
\bar{\epsilon}_{yz}^{i,A} &= -\frac{1}{2\sqrt{3}a}\left(-u_{B,i+\mathbf{a}_2}^z + u_{B,i+\mathbf{a}_3}^z\right).
\end{aligned} \tag{31}$$

Here, $\epsilon_{\alpha\beta}^{i,B}$ can be obtained by replacement $B \to A$ and $\mathbf{a}_i \to -\mathbf{a}_i$. The explicit expressions of the quadratic Hamiltonian describing the magnon-phonon interaction that includes a magnon operator and a phonon operator are shown in Appendix A.

III. BAND TOPOLOGY OF MAGNON-POLARONS

Here, we present the computational results for the band structure of the magnon-polaron bands and the corresponding topological transport properties of the magnon-polarons. In the numerical calculation, we include the second- and the third-nearest-neighbor exchanges (J_2 and J_3) in addition to the nearest-neighbor exchange (J) to accurately represent the magnon dynamics. In this paper, we utilize the magnetic parameter of $MnPS_3$ as it is known to exhibit a field-induced spin-flop transition at around 5.5 T [61]: $J = 1.54$ meV, $J_2 = 0.14$ meV, $J_3 = 0.36$ meV, $S = 5/2$ [53] and $KS = 7.25$ μeV. For the phonons, we use following parameters. The lattice constant is $a \approx 3.5$ Å [62], Mn ion mass is $M = 55$ u, and the spring constants are taken in agreement with the phonon spectrum of $MnPS_3$: $K_L = 300\,\mathrm{eV/nm^2}$, $K_L = 110\,\mathrm{eV/nm^2}$ and $K_Z = 50\,\mathrm{eV/nm^2}$ [63]. For the magnetoelastic constants, we use $B^\epsilon = B_{12}^\alpha = B_{22}^\alpha = B^\gamma = -0.84$ meV, resulting in $B^\epsilon/V \approx -1.2 \times 10^7\,\mathrm{erg/cm^3}$, which is comparable to Kittel's estimation for iron [46].

The magnon-polaron Hamiltonian in our model is expressed as

$$H = H_m + H_p + H_{mp} = \frac{1}{2}\sum_{\mathbf{k}} \psi_{\mathbf{k}}^\dagger \mathcal{H}_{\mathbf{k}} \psi_{\mathbf{k}}, \tag{32}$$

where $\psi_{\mathbf{k}} = (\psi_{m,\mathbf{k}}, \psi_{p,\mathbf{k}})$. Due to the complexity of our model Hamiltonian, which is a 16×16 matrix, analytical computation of the eigenvalue problem is challenging. In this context, we present numerical results for the band structure and the topological properties of the magnon-polarons.

The band topology is characterized by the Berry curvature of the Bogoliubov Hamiltonian [28],

$$\Omega_z^n(\mathbf{k}) = (\sigma_3)_{nn}(\sigma_3)_{mm} \sum_{n\neq m} \frac{-2\mathrm{Im}[\langle n|v_x|m\rangle\langle m|v_y|n\rangle]}{\left(\epsilon_{\mathbf{k}}^n - \epsilon_{\mathbf{k}}^m\right)^2 + \delta^2}, \tag{33}$$

where $v_i = \frac{1}{\hbar}\frac{\partial \mathcal{H}_{\mathbf{k}}}{\partial \mathbf{k}}$ is the velocity operator, $|n\rangle$ and $\epsilon_{\mathbf{k}}^n$ are the nth right eigenvector and corresponding eigenvalue of the Bogoliubov Hamiltonian, respectively. Here, we introduce a level broadening parameter δ, set to be 0 in this section. We consider finite level broadening in the thermal Hall transport calculation in Sec. IV. In this section, we employ the numerical algorithm proposed by Fukui, Hatsugai, and Suzuki [64] to efficiently compute the Chern number of the magnon-polaron bands.

1. Band topology in a collinear AFM state

In the collinear AFM state, the magnon-phonon interaction excludes the in-plane phonon amplitudes [41]. As the band topology remains unaffected by these in-plane phonon modes, we simplify the model by disregarding these modes. Consequently, we consider an 8×8 Bogoliubov Hamiltonian that includes two magnon modes ($a_{\mathbf{k}}$ and $b_{\mathbf{k}}$) and two out-of-plane phonon modes ($\bar{u}_{z,\mathbf{k}}^A$ and $\bar{u}_{z,\mathbf{k}}^B$) for the particle and hole sectors, respectively.

In Fig. 2, we depict the band structures for the collinear AFM phase in the presence of a perpendicular magnetic field ($B = 5$ T), both with and without magnon-phonon interaction. With finite magnon-phonon interaction, anticrossing band gaps emerge between magnon and phonon modes near Γ and $K(K')$ points [highlighted as shaded circles in Figs. 2(d) and 2(e)]. These gaps lead to the formation of topological magnon-polarons with finite Berry curvature in Figs. 3(a)–3(d).

We observe that under a sufficient magnetic field ($B = 5$ T), the (lower) magnon band touches the acoustic phonon band near the Γ point [Fig. 2(c)], resulting in the anticrossing gap [Fig. 2(e)] and finite Berry curvature [Figs. 3(a) and 3(b)] around this point. At low temperatures, the Berry curvature of the low-energy bands significantly contributes to the thermal Hall transport, as discussed in Sec. IV. However, if the magnetic field is not sufficiently large, the magnon band does not touch the phonon band, leading to negligible Berry curvature around Γ point (see Appendix B).

Additionally, the Berry curvatures remain finite in the vicinity of the $K(K')$ point [Figs. 3(a)–3(d)] due to the presence of the anticrossing gap in Fig. 2(d), contributing to thermal Hall transport at high temperatures. It is noteworthy that the magnon-phonon interaction introduces a barely

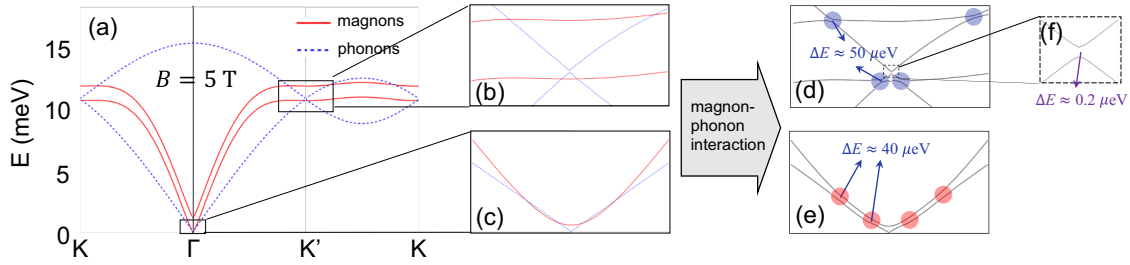

FIG. 2. Band structures of magnon and phonon modes in a collinear antiferromagnetic (AFM) state in the absence of magnon-phonon interaction (a)–(c) and in the presence of magnon-phonon interaction (d)–(f). In (d) and (e), anticrossing gaps that affect the thermal Hall effect at high and low temperatures are highlighted with blue and red shaded circles, respectively. A barely visible band gap between two phonon-like modes is numerically confirmed in (f). Here, we use $B^{\epsilon} = -0.84$ meV and $B = 5$ T.

visible band gap (about 0.2 μeV) between two phonon-like bands at the $K(K')$ point [Fig. 2(f)], inducing a large Berry curvature at this point. However, if we consider the finite-level broadening effect, the band topology at this slight anticrossing gap is strongly suppressed by the level broadening and does not affect the Hall transport.

2. *Band topology in a spin-flop state*

In the spin-flop state, the magnon-phonon interaction involves both in-plane and out-of-plane phonon amplitudes. In this case, we consider a 16×16 Bogoliubov Hamiltonian including two magnon modes and six phonon modes for the particle and hole sectors, respectively. In Fig. 4, we show the low-energy band structures for the spin-flop phase under the influence of a perpendicular magnetic field $B = 10$ T, both with and without magnon-phonon interaction.

Because $b \ll 6JS$ for $B = 10$ T, the spin canted angle is small ($\theta \approx 0.05$), and there is also a small band gap between the two magnonic bands. Similar to the collinear AFM case, the magnon-phonon interaction induces anticrossing gaps between magnon and phonon modes. In the spin-flop state, the gapless magnonic mode and the acoustic phonon modes converge at $\mathbf{k} = 0$, and the magnon-polaron band topology is not well-defined at this point. To establish a well-defined band topology theoretically, we introduce a sufficiently small easy-axis magnetic anisotropy along the bond direction, which should be present due to the lattice structure, but is higher-order anisotropy than the other terms in our magnetic Hamiltonian and therefore expected to induce negligible physical effects. Close to the Γ and K points, the magnonic mode couples with the phonon modes, resulting in the formation of anticrossing gaps [Figs. 4(c)–4(e) and 4(g)–4(i)]. Also, we numerically confirm the barely visible energy gaps (about $0.1 - 0.2$ μeV) between two phonon-like modes [Figs. 4(j)–4(l)], of which the Hall transport is strongly suppressed by the finite-level broadening. Here, we omit the in-plane optical phonon modes, because these high-energy phonons do not couple with the magnons, displaying trivial topology ($C_7 = C_8 = 0$).

In Fig. 5, we present the Berry curvatures and corresponding Chern numbers of the lowest six modes. Figures 4 and 5 illustrate one of our main findings: the exploration of the topological characteristics of the magnon-polaron, incorporating both in-plane and out-of-plane phonon modes in the AFM spin-flop state, which has not been addressed in previous studies. It is noteworthy that, in contrast to the collinear AFM case, the magnon-polaron gaps near the Γ point are very small (approximately 1 μeV) [Figs. 4(m) and 4(n)]. This suggests that the thermal Hall effect at low temperatures is negligible in the spin-flop phase. We note that the Berry curvature effect in the spin-flop phase primarily originates from the anticrossing gaps located far from the Γ point [highlighted as shaded circles in Figs. 4(g) and 4(h)], which correspond to high temperatures (10 meV ≈120 K). Therefore, we anticipate that the thermal Hall effect will increase with temperature for $T < 120$ K.

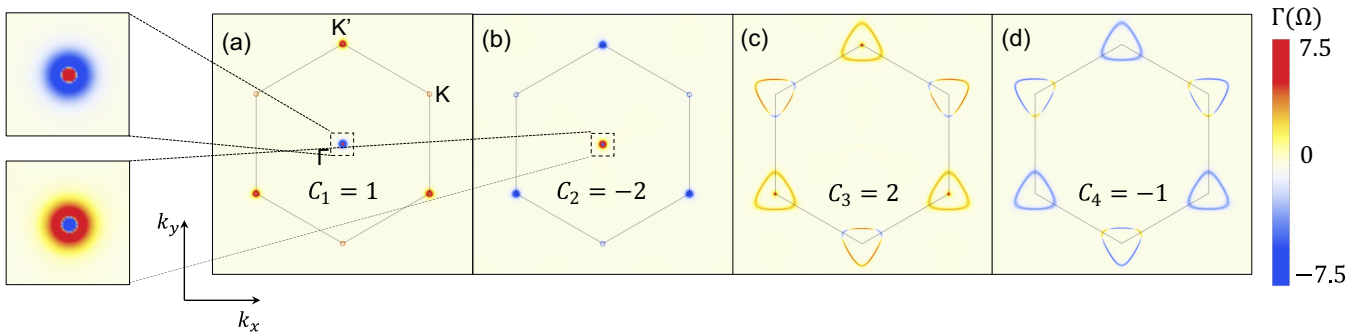

FIG. 3. Profiles of the log scale Berry curvature $\Gamma(\Omega) = \mathrm{sgn}(\Omega)\log(1 + |\Omega|)$ of the magnon-polaron bands (from low to high energies) in the collinear AFM phase. C_n ($n = 1 - 4$) denotes the corresponding Chern number of nth band. The hexagon represents the 1st Brillouin zone. Here, we use $B^{\epsilon} = -0.84$ meV and $B = 5$ T.

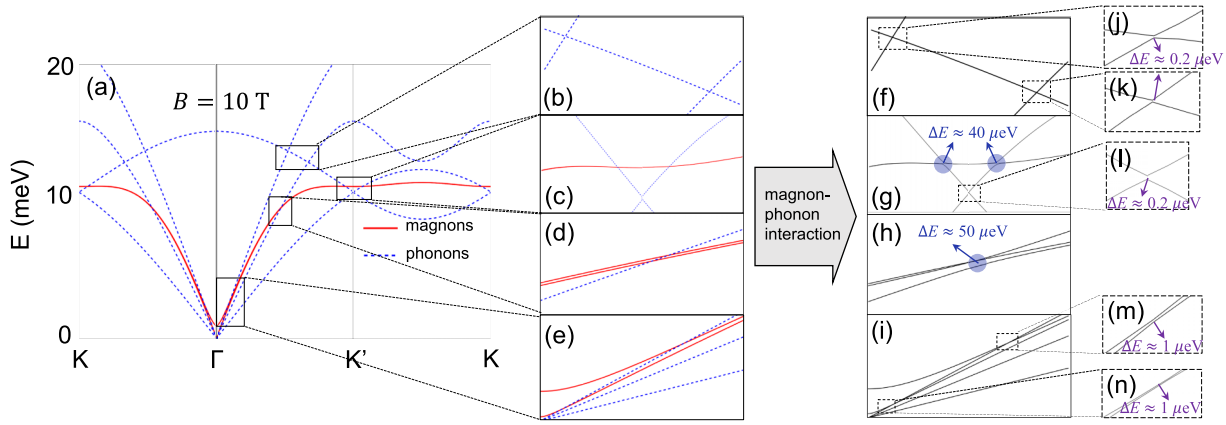

FIG. 4. Band structures of magnon and phonon modes in the spin-flop state in the absence of magnon-phonon interaction (a)–(e) and in the presence of magnon-phonon interaction (f)–(n). In (g), anticrossing gaps that affect the thermal Hall effect at high temperatures are highlighted with blue shaded circles. Barely visible band gaps are numerically confirmed in (j-n). Here, we use $B^{\epsilon} = B^{\alpha}_{12} = B^{\alpha}_{22} = B^{\gamma} = -0.84$ meV and $B = 10$ T.

IV. THERMAL HALL EFFECT

The topology of magnon-phonon hybrid excitations gives rise to the intrinsic thermal Hall effect. The Berry-curvature-induced thermal Hall conductivity is given by [21,65]

$$\kappa_{xy}^{2D} = -\frac{k_B^2 T}{\hbar V} \sum_{n,\mathbf{k}} [c_2(\rho_{n,\mathbf{k}}) - \pi^2/3]\Omega_z^n(\mathbf{k}), \tag{34}$$

where $c_2(\rho) = (1+\rho)\ln^2[(1+\rho)/\rho] - \ln^2\rho - 2\mathrm{Li}_2(-\rho)$, $\rho_{n,\mathbf{k}} = (e^{E_n(\mathbf{k})/k_BT} - 1)^{-1}$ is the Bose-Einstein distribution function with a zero chemical potential, k_B is the Boltzmann constant, T is the temperature, and $\mathrm{Li}_2(z)$ is the polylogarithm function. Here, we use the same parameters used in the previous section except for a constant level broadening parameter $\delta = 10$ μeV [66]. To convert two-dimensional conductivity to bulk conductivity, we employ the relation $\kappa_{xy} = \kappa_{xy}^{2D}/d$, with $d = 0.67$ nm representing the monolayer thickness of $MnPS_3$ [62,67]. In Fig. 6, a key outcome of our study, we illustrate the magnetic field and temperature dependence of the thermal Hall conductivity for magnon-polarons, considering both in-plane and out-of-plane lattice dynamics.

In the collinear AFM phase, the thermal Hall conductivity is positive and monotonically increases with the magnetic field at $T = 10$ K. However, at $T = 30$ and 50 K, the thermal Hall conductivity initially decreases with increasing B for $B < 5$ T, and subsequently increases with B for $B > 5$ T. For a clearer understanding, we show the band structures (near Γ point) and the Berry curvature profiles in the collinear AFM phase for different magnetic fields in the Appendix B. Due to the Zeeman interaction $E = g\mu_B BS_z$, the energy of the lower magnon band decreases as the magnetic field is increased. If the magnetic field is sufficiently large ($B \approx 5$ T), the (lower) magnon band touches the acoustic phonon band as depicted in Fig. 2(c). In this case, the anticrossing effect at the Γ point is maximized [Figs. 3(a) and 3(b)], resulting in a dominant contribution to the thermal Hall effect even at low temperatures. However, if the magnetic field B is not sufficiently large, the magnon band does not touch the phonon band, leading to negligible Berry curvature at the Γ point (see Fig. 7). In this case, the dominant contribution to the thermal Hall effect comes from the Berry curvature near the $K(K')$ points. As the energies corresponding to the $K(K')$ points are large (approximately, 10 meV ≈120 K), they contribute to thermal Hall transport primarily at high temperatures. Due to the opposite signs of Berry curvature at Γ and $K(K')$ points, the thermal Hall conductivity undergoes a sign change at certain magnetic field and temperature values.

In the spin-flop phase, as discussed in Sec. III, the magnon-polaron gaps near the Γ point are very small, resulting in negligible thermal Hall conductivity at low temperatures. Because the dominant contribution to the Berry curvature effect primarily originates from the high-energy anticrossing gaps

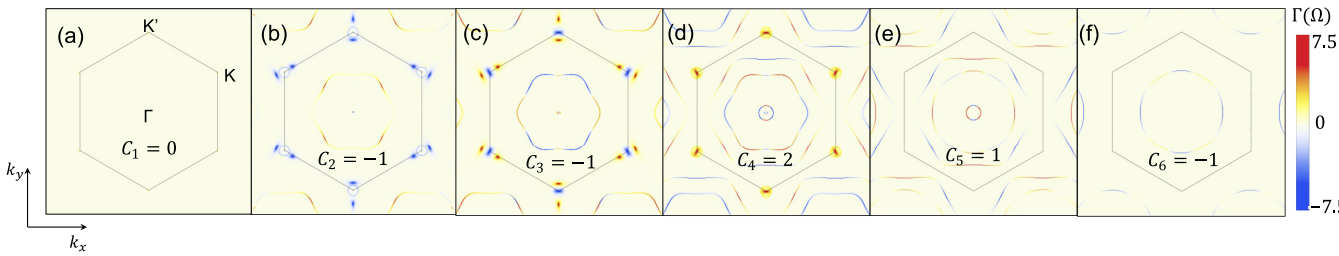

FIG. 5. Profiles of the log scale Berry curvature $\Gamma(\Omega) = \mathrm{sgn}(\Omega)\log(1+|\Omega|)$ of the magnon-polaron bands (from low to high energies) in the spin-flop phase. C_n ($n = 1-6$) denotes the corresponding Chern number of nth band. The hexagon represents the 1st Brillouin zone. Here, we use $B^{\epsilon} = B^{\alpha}_{12} = B^{\alpha}_{22} = B^{\gamma} = -0.84$ meV and $B = 10$ T.

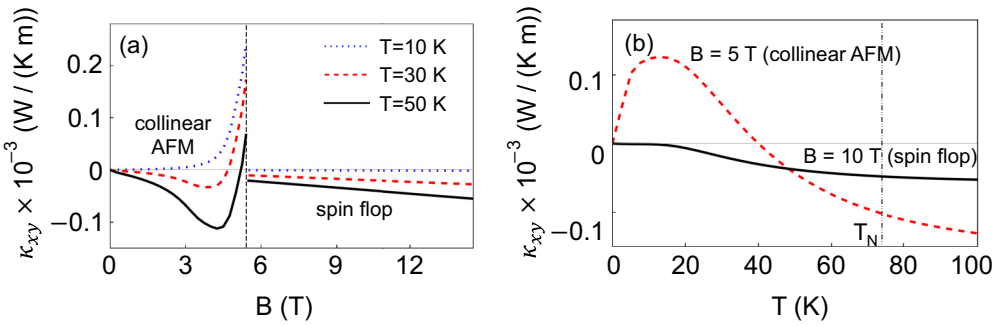

FIG. 6. Thermal Hall conductivity as a function of (a) an external magnetic field and (b) temperature. T_N denotes the Néel temperature of the $MnPS_3$. Although strictly speaking, magnons are defined well only below the Néel temperature, The calculation result is shown also above the Néel temperature to provide the qualitative temperature dependence of the thermal Hall conductivity for a broad range of temperatures.

located far from the Γ point, the thermal Hall conductivity increases as temperature rises and the high-energy states become occupied [see Fig. 6(b)]. Additionally, the external magnetic field increases the spin canted angle and differentiates the two magnon bands, leading to an increase in thermal Hall conductivity with the magnetic field [see Fig. 6(a)].

V. DISCUSSION

In this study, we explore the topological properties of magnon-polaron bands in a two-dimensional honeycomb antiferromagnetic insulator by varying an external magnetic field. We specifically investigate the impact of strain-dependent magnetic anisotropy, a common feature in magnetic materials, on the topological magnon-polarons. The magnetic phase transition from the collinear antiferromagnetic phase to the spin-flop phase induces a notable transformation in the magnon-polaron band structure and its associated topological properties. Consequently, the thermal Hall conductivity undergoes a change in sign and amplitude at the phase transition point. Our findings provide insights for interpreting experimental data on thermal Hall conductivity in two-dimensional antiferromagnetic materials.

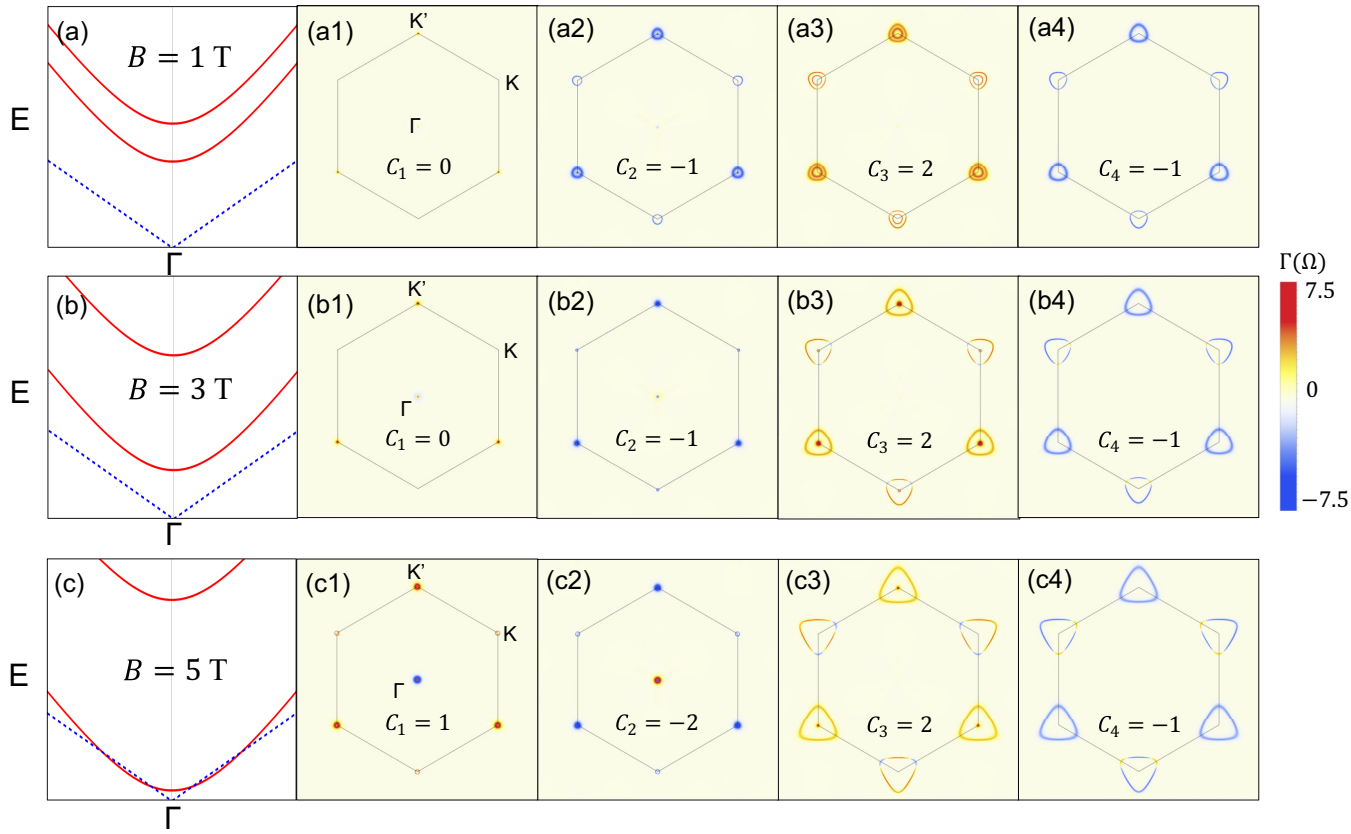

FIG. 7. The band structures near Γ point and the Berry curvature profiles in the collinear AFM phase for different magnetic fields.

ACKNOWLEDGMENTS

This work was supported by the Brain Pool Plus Program through the National Research Foundation of Korea funded by the Ministry of Science and ICT (2020H1D3A2A03099291) and the National Research Foundation of Korea funded by the Korea Government via the SRC Center for Quantum Coherence in Condensed Matter (RS-2023-00207732). G.G. acknowledges support by the National Research Foundation of Korea (NRF-2022R1C1C2006578). The work at SNU was supported by the Leading Researcher Program of the National Research Foundation of Korea (Grant No. 2020R1A3B2079375).

APPENDIX A: MAGNON-PHONON INTERACTION

1. Magnon-phonon interaction in collinear AFM state

In the collinear AFM state, off-diagonal components of the strain tensor involving out-of-plane phonon vibration only contributes to the magnetoelastic interaction to linear order in magnon amplitude. Explicitly, we have

$$H_{mp} = -\frac{B^{\epsilon}}{2}\sum_{\nu}\sum_{i\in\nu} S^{z}_{\nu}\left(S^{x}_{\nu}\epsilon^{\nu}_{xz} + S^{y}_{\nu}\epsilon^{\nu}_{yz} + \epsilon^{\nu}_{zx}S^{x}_{\nu} + \epsilon^{\nu}_{zy}S^{y}_{\nu}\right). \tag{A1}$$

By using Eq. (31) and taking the Fourier transformation with the Holstein Primakoff approach, we obtain

$$H_{mp} = \frac{\kappa_{\epsilon}}{2}\sum_{\mathbf{k}}\left[s^{*}_{x}\bar{u}^{B}_{z,-\mathbf{k}}\left(\frac{a_{\mathbf{k}}+a^{\dagger}_{-\mathbf{k}}}{\sqrt{2}}\right) + s^{*}_{y}\bar{u}^{B}_{z,-\mathbf{k}}\left(\frac{a_{\mathbf{k}}-a^{\dagger}_{-\mathbf{k}}}{\sqrt{2}i}\right) + s_{x}\bar{u}^{A}_{z,-\mathbf{k}}\left(\frac{b_{\mathbf{k}}+b^{\dagger}_{-\mathbf{k}}}{\sqrt{2}}\right) - s_{y}\bar{u}^{A}_{z,-\mathbf{k}}\left(\frac{b_{\mathbf{k}}-b^{\dagger}_{-\mathbf{k}}}{\sqrt{2}i}\right)\right] + \text{H.c.}, \tag{A2}$$

where $s_x = (-2e^{i\mathbf{k}\cdot\mathbf{a}_1} + e^{i\mathbf{k}\cdot\mathbf{a}_2} + e^{i\mathbf{k}\cdot\mathbf{a}_3})$, $s_y = \sqrt{3}(-e^{i\mathbf{k}\cdot\mathbf{a}_2} + e^{i\mathbf{k}\cdot\mathbf{a}_3})$ (in the low-$\mathbf{k}$ limit, $s_x \approx -3ik_x, s_y \approx -3ik_y$) and $\kappa_{\epsilon} = \frac{B^{\epsilon}S}{6a}\sqrt{\frac{\hbar S}{M\omega_0}}$. We note that the magnon-phonon interaction does not involve the in-plane phonon modes in the collinear AFM state.

2. Magnon-phonon interaction in spin-flop state

In the spin-flop phase, the sub-lattice dependent spin transformation (8) leads to

$$\begin{aligned} H_{mp} = &-S\sum_{\nu}\sum_{i\in\nu}(-1)^{\nu+1}\cos\theta\sin\theta\left[\left(E^{\nu}_{xx}-E^{\nu}_{zz}\right)S'^{x}_{\nu} + S'^{x}_{\nu}\left(E^{\nu}_{xx}-E^{\nu}_{zz}\right)\right] + (-1)^{\nu+1}\cos\theta\left(E^{\nu}_{xy}S'^{y}_{\nu} + S'^{y}_{\nu}E^{\nu}_{xy}\right) \\ &+ (\sin^2\theta - \cos^2\theta)\left(E^{\nu}_{xz}S'^{x}_{\nu} + S'^{x}_{\nu}E^{\nu}_{xz}\right) + \sin\theta\left(S'^{y}_{\nu}E^{\nu}_{yz} + E^{\nu}_{yz}S'^{y}_{\nu}\right). \end{aligned} \tag{A3}$$

In this case, the magnon-phonon interaction includes full in-plane and out-of-plane phonon modes. In terms of dimensionless operators, the momentum space representation of the magnon-phonon interaction is

$$\begin{aligned} H_{mp} = &\sin 2\theta\sum_{\mathbf{k}}\left[\kappa_{-}s^{*}_{x}u^{x}_{B,-\mathbf{k}}\left(\frac{a_{\mathbf{k}}+a^{\dagger}_{-\mathbf{k}}}{\sqrt{2}}\right) + \kappa_{+}s^{*}_{y}u^{y}_{B,-\mathbf{k}}\left(\frac{a_{\mathbf{k}}+a^{\dagger}_{-\mathbf{k}}}{\sqrt{2}}\right)\right. \\ &\left. - \kappa_{-}s_{x}u^{x}_{A,-\mathbf{k}}\left(\frac{b_{\mathbf{k}}+b^{\dagger}_{-\mathbf{k}}}{\sqrt{2}}\right) - \kappa_{+}s_{y}u^{y}_{A,-\mathbf{k}}\left(\frac{b_{\mathbf{k}}+b^{\dagger}_{-\mathbf{k}}}{\sqrt{2}}\right)\right] \\ &+ \frac{\kappa_{\gamma}}{2}\cos\theta\sum_{\mathbf{k}}\left\{\left(s^{*}_{x}u^{y}_{B,-\mathbf{k}} + s^{*}_{y}u^{x}_{B,-\mathbf{k}}\right)\left(\frac{a_{\mathbf{k}}-a^{\dagger}_{-\mathbf{k}}}{\sqrt{2}i}\right) - \left(s_{x}u^{y}_{A,-\mathbf{k}} + s_{y}u^{x}_{A,-\mathbf{k}}\right)\left(\frac{b_{\mathbf{k}}-b^{\dagger}_{-\mathbf{k}}}{\sqrt{2}i}\right)\right\} \\ &- \frac{\kappa_{\epsilon}}{2}\cos 2\theta\sum_{\mathbf{k}}\left[s^{*}_{x}u^{z}_{B,-\mathbf{k}}\left(\frac{a_{\mathbf{k}}+a^{\dagger}_{-\mathbf{k}}}{\sqrt{2}}\right) + s_{x}u^{z}_{A,-\mathbf{k}}\left(\frac{b_{\mathbf{k}}+b^{\dagger}_{-\mathbf{k}}}{\sqrt{2}}\right)\right] \\ &+ \frac{\kappa_{\epsilon}}{2}\sin\theta\sum_{\mathbf{k}}\left[s^{*}_{y}u^{z}_{B,-\mathbf{k}}\left(\frac{a_{\mathbf{k}}-a^{\dagger}_{-\mathbf{k}}}{\sqrt{2}i}\right) + s_{y}u^{z}_{A,-\mathbf{k}}\left(\frac{b_{\mathbf{k}}-b^{\dagger}_{-\mathbf{k}}}{\sqrt{2}i}\right)\right] + \text{H.c.}, \end{aligned} \tag{A4}$$

where $\kappa_{\gamma} = \frac{B^{\gamma}S}{6a}\sqrt{\frac{\hbar S}{M\omega_0}}$ and $\kappa_{\pm} = \frac{B_{\pm}S}{6a}\sqrt{\frac{\hbar S}{M\omega_0}}$ with $B_{\pm} = \frac{1}{4}(-2\sqrt{3}B^{\alpha}_{12} + B^{\alpha}_{22} \pm B^{\gamma})$.

APPENDIX B: BAND STRUCTURES AND BERRY CURVATURES WITH VARIOUS MAGNETIC FIELDS IN THE COLLINEAR AFM PHASE

In Fig. 7, we present the band structures near Γ point and Berry curvature profiles in the collinear AFM phase for different magnetic fields.

[1] M. A. McGuire, H. Dixit, V. R. Cooper, and B. C. Sales, Coupling of crystal structure and magnetism in the layered, ferromagnetic insulator CrI_3, Chem. Mater. **27**, 612 (2015).

[2] W.-B. Zhang, Q. Qu, P. Zhu, and C.-H. Lam, Robust intrinsic ferromagnetism and half semiconductivity in stable two-dimensional single-layer chromium trihalides, J. Mater. Chem. C **3**, 12457 (2015).

[3] J.-G. Park, Opportunities and challenges of 2D magnetic van der Waals materials: Magnetic graphene? J. Phys.: Condens. Matter **28**, 301001 (2016).

[4] J.-U. Lee, S. Lee, J. H. Ryoo, S. Kang, T. Y. Kim, P. Kim, C.-H. Park, J.-G. Park, and H. Cheong, Ising-type magnetic ordering in atomically thin $FePS_3$, Nano Lett. **16**, 7433 (2016).

[5] C. Gong, L. Li, Z. Li, H. Ji, A. Stern, Y. Xia, T. Cao, W. Bao, C. Wang, Y. Wang *et al.*, Discovery of intrinsic ferromagnetism in two-dimensional van der Waals crystals, Nature (London) **546**, 265 (2017).

[6] B. Huang, G. Clark, E. Navarro-Moratalla, D. R. Klein, R. Cheng, K. L. Seyler, D. Zhong, E. Schmidgall, M. A. McGuire, D. H. Cobden *et al.*, Layer-dependent ferromagnetism in a van der Waals crystal down to the monolayer limit, Nature (London) **546**, 270 (2017).

[7] K. S. Burch, D. Mandrus, and J.-G. Park, Magnetism in two-dimensional van der Waals materials, Nature (London) **563**, 47 (2018).

[8] Y. Deng, Y. Yu, Y. Song, J. Zhang, N. Z. Wang, Z. Sun, Y. Yi, Y. Z. Wu, S. Wu, J. Zhu *et al.*, Gate-tunable room-temperature ferromagnetism in two-dimensional Fe_3GeTe_2, Nature (London) **563**, 94 (2018).

[9] Z. Fei, B. Huang, P. Malinowski, W. Wang, T. Song, J. Sanchez, W. Yao, D. Xiao, X. Zhu, A. F. May *et al.*, Two-dimensional itinerant ferromagnetism in atomically thin Fe_3GeTe_2, Nat. Mater. **17**, 778 (2018).

[10] D. J. O'Hara, T. Zhu, A. H. Trout, A. S. Ahmed, Y. K. Luo, C. H. Lee, M. R. Brenner, S. Rajan, J. A. Gupta, D. W. McComb, and R. K. Kawakami, Room temperature intrinsic ferromagnetism in epitaxial manganese selenide films in the monolayer limit, Nano Lett. **18**, 3125 (2018).

[11] M. Gibertini, M. Koperski, A. F. Morpurgo, and K. S. Novoselov, Magnetic 2D materials and heterostructures, Nat. Nanotechnol. **14**, 408 (2019).

[12] K. Kim, S. Y. Lim, J. Kim, J.-U. Lee, S. Lee, P. Kim, K. Park, S. Son, C.-H. Park, J.-G. Park, and H. Cheong, Antiferromagnetic ordering in van der Waals 2D magnetic material $MnPS_3$ probed by Raman spectroscopy, 2D Mater. **6**, 041001 (2019).

[13] A. V. Chumak, V. I. Vasyuchka, A. A. Serga, and B. Hillebrands, Magnon spintronics, Nat. Phys. **11**, 453 (2015).

[14] M. Maldovan, Sound and heat revolutions in phononics, Nature (London) **503**, 209 (2013).

[15] H. Katsura, N. Nagaosa, and P. A. Lee, Theory of the thermal Hall effect in quantum magnets, Phys. Rev. Lett. **104**, 066403 (2010).

[16] J. H. Han and H. Lee, Spin chirality and Hall-like transport phenomena of spin excitations, J. Phys. Soc. Jpn. **86**, 011007 (2017).

[17] B. Göbel, A. Mook, J. Henk, and I. Mertig, Unconventional topological Hall effect in skyrmion crystals caused by the topology of the lattice, Phys. Rev. B **95**, 094413 (2017).

[18] S. A. Díaz, J. Klinovaja, and D. Loss, Topological magnons and edge states in antiferromagnetic skyrmion crystals, Phys. Rev. Lett. **122**, 187203 (2019).

[19] S. K. Kim, K. Nakata, D. Loss, and Y. Tserkovnyak, Tunable magnonic thermal Hall effect in skyrmion crystal phases of ferrimagnets, Phys. Rev. Lett. **122**, 057204 (2019).

[20] Y. Onose, T. Ideue, H. Katsura, Y. Shiomi, N. Nagaosa, and Y. Tokura, Observation of the magnon Hall effect, Science **329**, 297 (2010).

[21] R. Matsumoto and S. Murakami, Theoretical prediction of a rotating magnon wave packet in ferromagnets, Phys. Rev. Lett. **106**, 197202 (2011).

[22] L. Zhang, J. Ren, J.-S. Wang, and B. Li, Topological magnon insulator in insulating ferromagnet, Phys. Rev. B **87**, 144101 (2013).

[23] A. Mook, J. Henk, and I. Mertig, Edge states in topological magnon insulators, Phys. Rev. B **90**, 024412 (2014).

[24] S. K. Kim, H. Ochoa, R. Zarzuela, and Y. Tserkovnyak, Realization of the Haldane-Kane-Mele model in a system of localized spins, Phys. Rev. Lett. **117**, 227201 (2016).

[25] R. Cheng, S. Okamoto, and D. Xiao, Spin Nernst effect of magnons in collinear antiferromagnets, Phys. Rev. Lett. **117**, 217202 (2016).

[26] S. A. Owerre, A first theoretical realization of honeycomb topological magnon insulator, J. Phys.: Condens. Matter **28**, 386001 (2016).

[27] V. A. Zyuzin and A. A. Kovalev, Magnon spin Nernst effect in antiferromagnets, Phys. Rev. Lett. **117**, 217203 (2016).

[28] B. Li, S. Sandhoefner, and A. A. Kovalev, Intrinsic spin Nernst effect of magnons in a noncollinear antiferromagnet, Phys. Rev. Res. **2**, 013079 (2020).

[29] L. Sheng, D. N. Sheng, and C. S. Ting, Theory of the phonon Hall effect in paramagnetic dielectrics, Phys. Rev. Lett. **96**, 155901 (2006).

[30] Yu. Kagan and L. A. Maksimov, Anomalous Hall effect for the phonon heat conductivity in paramagnetic dielectrics, Phys. Rev. Lett. **100**, 145902 (2008).

[31] L. Zhang, J. Ren, J.-S. Wang, and B. Li, Topological nature of the phonon Hall effect, Phys. Rev. Lett. **105**, 225901 (2010).

[32] B. Flebus and A. H. MacDonald, Charged defects and phonon Hall effects in ionic crystals, Phys. Rev. B **105**, L220301 (2022).

[33] X.-Q. Sun, J.-Y. Chen, and S. A. Kivelson, Large extrinsic phonon thermal Hall effect from resonant scattering, Phys. Rev. B **106**, 144111 (2022).

[34] H. Guo, D. G. Joshi, and S. Sachdev, Resonant thermal Hall effect of phonons coupled to dynamical defects, Proc. Natl. Acad. Sci. USA **119**, e2215141119 (2022).

[35] R. Takahashi and N. Nagaosa, Berry curvature in magnon-phonon hybrid systems, Phys. Rev. Lett. **117**, 217205 (2016).

[36] X. Zhang, Y. Zhang, S. Okamoto, and D. Xiao, Thermal Hall effect induced by magnon-phonon interactions, Phys. Rev. Lett. **123**, 167202 (2019).

[37] S. Park, N. Nagaosa, and B.-J. Yang, Thermal Hall effect, spin Nernst effect, and spin density induced by a thermal gradient in collinear ferrimagnets from magnon–phonon interaction, Nano Lett. **20**, 2741 (2020).

[38] H. Zhang, C. Xu, C. Carnahan, M. Sretenovic, N. Suri, D. Xiao, and X. Ke, Anomalous thermal Hall effect in an insulating van der Waals magnet, Phys. Rev. Lett. **127**, 247202 (2021).

[39] S. Bao, Z.-L. Gu, Y. Shangguan, Z. Huang, J. Liao, X. Zhao, B. Zhang, Z.-Y. Dong, W. Wang, R. Kajimoto *et al.*, Direct observation of topological magnon polarons in a multiferroic material, Nat. Commun. **14**, 6093 (2023).

[40] G. Go, S. K. Kim, and K.-J. Lee, Topological magnon-phonon hybrid excitations in two-dimensional ferromagnets with tunable Chern numbers, Phys. Rev. Lett. **123**, 237207 (2019).

[41] S. Zhang, G. Go, K.-J. Lee, and S. K. Kim, SU(3) topology of magnon-phonon hybridization in 2D antiferromagnets, Phys. Rev. Lett. **124**, 147204 (2020).

[42] P. Shen and S. K. Kim, Magnetic field control of topological magnon-polaron bands in two-dimensional ferromagnets, Phys. Rev. B **101**, 125111 (2020).

[43] N. Bazazzadeh, M. Hamdi, S. Park, A. Khavasi, S. M. Mohseni, and A. Sadeghi, Magnetoelastic coupling enabled tunability of magnon spin current generation in two-dimensional antiferromagnets, Phys. Rev. B **104**, L180402 (2021).

[44] H. Huang and Z. Tian, Topological phonon-magnon hybrid excitations in a two-dimensional honeycomb ferromagnet, Phys. Rev. B **104**, 064305 (2021).

[45] G. Go and S. K. Kim, Tunable large spin Nernst effect in a two-dimensional magnetic bilayer, Phys. Rev. B **106**, 125103 (2022).

[46] C. Kittel, Physical theory of ferromagnetic domains, Rev. Mod. Phys. **21**, 541 (1949).

[47] C. Kittel, Interaction of spin waves and ultrasonic waves in ferromagnetic crystals, Phys. Rev. **110**, 836 (1958).

[48] E. Callen and H. B. Callen, Magnetostriction, forced magnetostriction, and anomalous thermal expansion in ferromagnets, Phys. Rev. **139**, A455 (1965).

[49] S. Liu, A. G. del Águila, D. Bhowmick, C. K. Gan, T. Thu Ha Do, M. A. Prosnikov, D. Sedmidubský, Z. Sofer, P. C. M. Christianen, P. Sengupta, and Q. Xiong, Direct observation of magnon-phonon strong coupling in two-dimensional antiferromagnet at high magnetic fields, Phys. Rev. Lett. **127**, 097401 (2021).

[50] J. Luo, S. Li, Z. Ye, R. Xu, H. Yan, J. Zhang, G. Ye, L. Chen, D. Hu, X. Teng *et al.*, Evidence for topological magnon–phonon hybridization in a 2D antiferromagnet down to the monolayer limit, Nano Lett. **23**, 2023 (2023).

[51] C. Xu, C. Carnahan, H. Zhang, M. Sretenovic, P. Zhang, D. Xiao, and X. Ke, Thermal Hall effect in a van der Waals triangular magnet $FeCl_2$, Phys. Rev. B **107**, L060404 (2023).

[52] N. Li, R. R. Neumann, S. K. Guang, Q. Huang, J. Liu, K. Xia, X. Y. Yue, Y. Sun, Y. Y. Wang, Q. J. Li *et al.*, Magnon-polaron driven thermal Hall effect in a Heisenberg-Kitaev antiferromagnet, Phys. Rev. B **108**, L140402 (2023).

[53] A. R. Wildes, B. Roessli, B. Lebech, and K. W. Godfrey, Spin waves and the critical behaviour of the magnetization in, J. Phys.: Condens. Matter **10**, 6417 (1998).

[54] N. Sivadas, M. W. Daniels, R. H. Swendsen, S. Okamoto, and D. Xiao, Magnetic ground state of semiconducting transition-metal trichalcogenide monolayers, Phys. Rev. B **91**, 235425 (2015).

[55] A. N. Bogdanov, A. V. Zhuravlev, and U. K. Rößler, Spin-flop transition in uniaxial antiferromagnets: Magnetic phases, reorientation effects, and multidomain states, Phys. Rev. B **75**, 094425 (2007).

[56] R. Ganesh, D. N. Sheng, Y.-J. Kim, and A. Paramekanti, Quantum paramagnetic ground states on the honeycomb lattice and field-induced Néel order, Phys. Rev. B **83**, 144414 (2011).

[57] S. Foner, High-field antiferromagnetic resonance in Cr_2O_3, Phys. Rev. **130**, 183 (1963).

[58] J. Li, C. B. Wilson, R. Cheng, M. Lohmann, M. Kavand, W. Yuan, M. Aldosary, N. Agladze, P. Wei, M. S. Sherwin, and J. Shi, Spin current from sub-terahertz-generated antiferromagnetic magnons, Nature (London) **578**, 70 (2020).

[59] L. A. Falkovsky, Phonon dispersion in graphene, J. Exp. Theor. Phys. **105**, 397 (2007).

[60] S. L. Holm, A. Kreisel, T. K. Schäffer, A. Bakke, M. Bertelsen, U. B. Hansen, M. Retuerto, J. Larsen, D. Prabhakaran, P. P. Deen *et al.*, Magnetic ground state and magnon-phonon interaction in multiferroic *h*-$YMnO_3$, Phys. Rev. B **97**, 134304 (2018).

[61] G. Long, H. Henck, M. Gibertini, D. Dumcenco, Z. Wang, T. Taniguchi, K. Watanabe, E. Giannini, and A. F. Morpurgo, Persistence of magnetism in atomically thin $MnPS_3$ crystals, Nano Lett. **20**, 2452 (2020).

[62] G. Ouvrard, R. Brec, and J. Rouxel, Structural determination of some MPS_3 layered phases (M = Mn, Fe, Co, Ni and Cd), Mater. Res. Bull. **20**, 1181 (1985).

[63] J. Yang, Y. Zhou, Q. Guo, Y. Dedkov, and E. Voloshina, Electronic, magnetic and optical properties of $MnPX_3$ (X = S, Se) monolayers with and without chalcogen defects: A first-principles study, RSC Adv. **10**, 851 (2020).

[64] T. Fukui, Y. Hatsugai, and H. Suzuki, Chern numbers in discretized Brillouin zone: Efficient method of computing (spin) Hall conductances, J. Phys. Soc. Jpn. **74**, 1674 (2005).

[65] R. Matsumoto, R. Shindou, and S. Murakami, Thermal Hall effect of magnons in magnets with dipolar interaction, Phys. Rev. B **89**, 054420 (2014).

[66] Here, we assume that the level broadening effect is dominated by the Gilbert damping $\delta = 2\alpha\epsilon$, where α is the Gilbert damping parameter and ϵ is the energy of the magnon band. In this work, we consider the constant level broadening by taking $\alpha = 0.005$ and $\epsilon = 5\,\text{meV}$, so that $\delta = 10\,\mu\text{eV}$.

[67] S. Y. Lim, K. Kim, S. Lee, J.-G. Park, and H. Cheong, Thickness dependence of antiferromagnetic phase transition in Heisenberg-type $MnPS_3$, Curr. Appl. Phys. **21**, 1 (2021).